

Simulation of a rotating drum heat exchanger for latent heat storage using a quasistationary analytical approach and a numerical transient finite difference scheme

Jonas Tombrink, Dan Bauer

German Aerospace Center (DLR), Institute of Engineering Thermodynamics

Pfaffenwaldring 38-40, 70569 Stuttgart, Germany

Phone: +49-711-6862-8835, e-mail: jonas.tombrink@dlr.de

Abstract

With the concept of the rotating drum heat exchanger, latent heat can be released with a high and constant surface specific heat flux. Phase change material (PCM) solidifies on the outer surface of a drum, which is steadily removed by a fixed scraper during rotation. Two novel calculation approaches for determining the heat transfer and the layer thickness for a rotating drum heat exchanger are developed and validated with existing experimental data. This includes the identification of correlations for the thickness of the adhering liquid layer after the surface emerges from the liquid PCM and the local surface coefficient of heat transfer on the outside of a partially immersed rotating drum. While a calculation approach based on the quasistationary simplification underestimates the experimentally measured heat transfer for rotational speeds above 4 min^{-1} by 31 % on average, a detailed transient numerical simulation based on a time-varying finite difference scheme reproduces the experimentally measured heat transfer with an accuracy of 8 % on average. By applying the transient numerical simulation to a rotating drum heat exchanger using sodium nitrate as the PCM, a surface specific heat transfer based on the entire drum surface of up to $400 \text{ kW}\cdot\text{m}^{-2}$ can be assumed, showing the high potential of the rotating drum heat exchanger for industrial and power plant applications.

Keywords

Active Latent Heat Thermal Energy Storage; Rotating Drum; Solidification; Time Varied Finite Difference Method; Quasistationary Calculation; Phase Change Material

Highlights

- Simulation of a rotating drum heat exchanger for latent heat storage
- Comparison of quasistationary simplification and detailed numerical investigation
- Reproduction of experimentally measured heat transfer with an accuracy of 8 % on average
- Identification of a heat transfer correlation for partially immersed cylinders
- Heat transfer potential of up to $400 \text{ kW}\cdot\text{m}^{-2}$ when using NaNO_3 as PCM

Nomenclature

Latin

a	thermal diffusivity, $[a] = \text{m}^2 \cdot \text{s}^{-1}$
c_p	heat capacity at constant pressure, $[c_p] = \text{J} \cdot \text{kg}^{-1} \cdot \text{K}^{-1}$
d	diameter, $[d] = \text{m}$
g	gravimetric acceleration, $[g] = \text{m} \cdot \text{s}^{-2}$
h	surface coefficient of heat transfer, $[h] = \text{W} \cdot \text{m}^{-2} \cdot \text{K}^{-1}$
K	coefficient of heat transfer, $[K] = \text{W} \cdot \text{m}^{-2} \cdot \text{K}^{-1}$
k	thermal conductivity, $[k] = \text{W} \cdot \text{m}^{-1} \cdot \text{K}^{-1}$
L	specific latent heat, $[L] = \text{J} \cdot \text{kg}^{-1}$
n	rotational speed, $[n] = \text{s}^{-1}$
\dot{q}	surface-specific heat flux, $[\dot{q}] = \text{W} \cdot \text{m}^{-2}$
s	thickness, $[s] = \text{m}$
T	thermodynamic temperature, $[T] = \text{K}$
t	time, $[t] = \text{s}$
u	velocity, $[u] = \text{m} \cdot \text{s}^{-1}$
x	(specific) length, $[x] = \text{m}$

Greek

η	dynamic viscosity, $[\eta] = \text{Pa} \cdot \text{s}$
Θ	(immersing) angle, $[\Theta] = ^\circ \text{deg}$
k	thermal conductivity, $[k] = \text{W} \cdot \text{m}^{-1} \cdot \text{K}^{-1}$
ϱ	density, $[\varrho] = \text{kg} \cdot \text{m}^{-3}$
σ	surface tension, $[\sigma] = \text{N} \cdot \text{m}^{-1}$

Mathematical Symbols

∂	partial differential
Δ	finite difference
d	differential

Dimensionless Numbers

Nu	Nusselt number, $\text{Nu} = h \cdot x \cdot k^{-1}$
Re	Reynolds number, $\text{Re} = \varrho \cdot v \cdot x \cdot \eta^{-1}$
Pr	Prandtl number, $\text{Pr} = \eta \cdot c_p \cdot k^{-1}$
Bi	Biot number, $\text{Bi} = h \cdot x \cdot k^{-1}$

Sub-/Superscripts

0	initial value
$\bar{}$	median
adh	adhesion
amb	ambient
HTF	Heat Transfer Fluid
h	hydraulic
i	iteration indices / inside
k	time step
l	liquid
m	melting
min	minimum
n	node/boundary
o	outer/outside
PCM	Phase Change Material
s	solid/boundary steel-PCM
x	local

1 Introduction

With latent heat thermal energy storages, thermal energy can be stored with increased storage density by utilizing the phase change of a phase change material (PCM), typically from liquid to solid state. During the discharge process of latent heat thermal energy storages, a layer of solidified PCM grows on the heat exchanger wall. Since the thermal conductivity of most cost-effective PCM is low, the growing solidified layer decreases the heat transfer depending on the state of discharge. This results in a time-dependent heat transfer during the discharge process. Beside other concepts summarized in [1], the concept of the rotating drum heat exchanger overcomes this limitation by a continuously scraped surface. The principle of the rotating drum heat exchanger is shown in Figure 1. Figure 2 shows a picture of the experimental test rig examined in [1], which also served as prove of concept. Thereby, a rotating drum is partially immersed in liquid PCM. A heat transfer fluid (HTF) passes through the inner side of the drum and extracts thermal energy from the outer PCM. The HTF can be either a single-phase fluid but rather an evaporating fluid. If the temperature of the HTF is below the melting point of the PCM used, the liquid PCM solidifies on the outside of the drum. The solidified PCM is moved out of the liquid PCM by the rotation of the drums surface and scraped off by a stationary scraper. The scraped PCM can be stored in a separate tank to achieve a complete separation of the power and capacity of the storage system. At the point of emergence, liquid PCM adheres to the surface, which solidifies after the surface has left the liquid PCM, as shown in Figure 3. This increases the surface area where solidification occurs. In the case of an HTF temperature above the melting temperature of the PCM, the rotating drum can also be used for the purely convective transfer of sensible heat. In this case, no solidification occurs. The concept is introduced and described in full detail in [1] and [2]. Compared to state-of-the-art two-tank molten salt storage systems commonly used in large scale Concentrated Solar Power Plants, the storage density of a storage system based on the rotating drum can be increased by the phase change enthalpy of the storage material. Thus, compared to a sensible molten salt thermal energy storage using pure sodium nitrate as storage material in the temperature range between 350 °C and 550 °C, the demand of storage material can be reduced by about 40 % when utilizing the phase change enthalpy as well as the temperature range from the melting temperature at 306 °C up to 550 °C [3]. This results in a cost reduction of both the storage material as well as the storage tanks. Another essential characteristic of latent heat thermal energy storages is their isothermal temperature level during the phase change process. This enables an almost isothermal charging and discharging of thermal energy storages. This is a key element for the success of systems where the exergetic losses are crucial for the efficiency of the system, such as in a certain variant of Carnot batteries [4], [5]. Furthermore, the provision of climate-neutral thermal energy for industrial processes, which is currently mainly based on fossil fuels, is becoming more in focus. Within the EU 28 states, the demand of thermal energy within the temperature range of

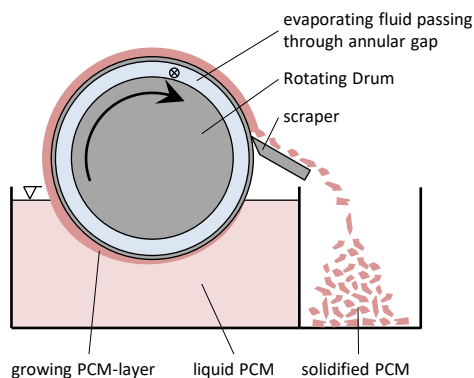


Figure 1: Principle of the rotating drum heat exchanger



Figure 2: Figure of the experimental test rig examined in [1]

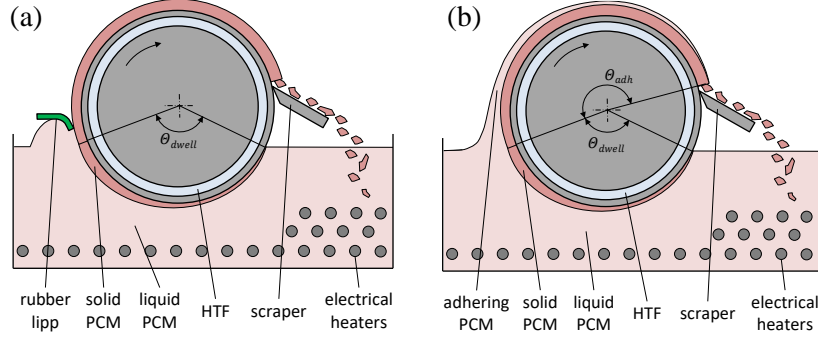


Figure 3: Illustration of the rotating drum heat exchanger a) without adhesion b) with adhesion

200 – 400 °C amounts to 2200 PJ per year, which corresponds to about 5% of the final energy demand across all sectors [6]. Steam is the most important carrier of thermal energy within this temperature range [7]. With a heat storage system based on the rotating drum heat exchanger, this demand can be met on demand by fluctuating renewable energy sources, either directly in the form of heat or by electrical energy using a heat pump or resistance heating elements.

The rotating drum has been experimentally investigated using the low temperature PCM decanoic acid. The experimental results are presented in [1]. Currently, specific calculation approaches for determining the heat transfer of a rotating drum heat exchanger are quite limited within the literature. Within this research, two novel calculation approaches for the calculation of the effective heat transfer as well as the layer thickness of the solidified PCM are developed and verified by the experimental results. Both, one based on the quasistationary calculation approach and one detailed transient numerical simulation, based on the finite difference method, are compared with each other and investigated for their applicability on the rotating drum heat exchanger. The main objective of this research is to obtain a calculation tool for the discharge performance of a heat storage system based on the rotating drum. The calculation tool should be applicable for the optimization and dimensioning of a high-temperature rotating drum heat exchanger and the uncertainties in the calculation should be estimable.

2 Description of the modelling approaches

Within this section, two different calculation approaches for the rotating drum heat exchangers are introduced. Both calculation approaches contain models for the heat transfer coefficients at the outer and inner side of the rotating drum and for the thickness of the adhering liquid PCM when the surface is emerged from the liquid PCM, which are identified in the sections 2.1 – 2.3. This is followed by the so called quasistationary calculation approach in section 2.4 and the introduction of a detailed transient numerical simulation in section 2.5.

2.1 Heat transfer coefficients at the outer side of the rotating cylinder

The heat transfer coefficient at the outer surface of the rotating drum is calculated by empirical correlations. For the heat transfer coefficient of a rotating cylinder completely surrounded by one medium, there are several correlations available in the literature e.g. in [8-11]. For a partially immersed rotating drum, no specific correlation could be identified by the authors. Nevertheless, the local surface-specific heat transfer coefficient can be compared to a continuously moving flat surface within a quiescent medium. According to [12] the following expression can be used for laminar conditions

$$\frac{Nu_x}{\sqrt{Re_x \cdot Pr}} = f(Pr) \quad (1)$$

Further research on a continuously moving plane surface is also carried out by [13] and [14] with the same results for the laminar conditions. Here, $f(Pr)$ is found by a numerical solution and is 0.4174 at

$Pr = 0.7$ for the ambient air. For decanoic acid, used in [1] for the experimental study, the Prandtl-Number is 88.72. The value of $f(Pr = 88.72)$ is found to be 0.5531 by linear interpolation of the data given in [13] between $Pr = 30$ and $Pr = 100$. In the same way, $f(Pr = 6.4704)$ is determined to be 0.521 for sodium nitrate, later used in Section 4. The local Reynolds-Number Re_x and the local Nusselt-Number Nu_x are determined with the length x , which is the arc length from the point of immersion or emersion to the certain position, by

$$Re_x = \frac{\rho \cdot u \cdot x}{\eta} \quad (2)$$

and

$$Nu_x = \frac{h_x \cdot x}{k}. \quad (3)$$

The local surface-specific heat transfer coefficient h_x can be calculated by rearranging Equation (3). Expression (1) is also valid for a rotating cylinder, which is used in [12] for experimental validation. The critical Reynolds-Number in the given case is $5 \cdot 10^5$, which is not exceeded within the experimental data for the validation.

2.2 Surface-specific heat transfer coefficient at the annular gap within the cylinder

At the inner side of the rotating drum, a HTF passes through an annular gap, as illustrated in Figure 1 and Figure 3. The surface-specific heat transfer coefficient at the inner side of the outer cylinder is therefore calculated by an empirical correlation by Gnielinski given in [15]. The Reynolds-Number in this case is defined with the hydraulic diameter

$$d_h = d_o - d_i \quad (4)$$

with the inner diameter of the outer tube d_o and the outer diameter of the inner tube d_i . The surface-specific heat transfer coefficient for water as HTF and the geometrical properties of the rotating drum as given in [1] can be determinate to be $4175 \text{ W} \cdot \text{m}^{-2} \cdot \text{K}^{-1}$. In case of an evaporating medium, the determination of a surface-specific heat transfer coefficient is highly complex and depends on several parameters. Therefore, a generalized value of $15\,000 \text{ W} \cdot \text{m}^{-2} \cdot \text{K}^{-1}$ is used in this study. Details for a detailed investigation of the surface-specific heat transfer coefficient for a boiling HTF can be found in [16]. For the specific properties of water, the data given in [17] are used.

2.3 Adhering liquid at a surface released from a tub

The liquid PCM layer which adheres at the surface of the solidified PCM when it is removed from the tub can be considered as a classical Landau-Levich Problem. For a plate vertically withdrawn from a liquid, the layer thickness s_{adh} of the remaining liquid PCM can be calculated according to Landau and Levich [18] by

$$s_{adh} = 0,93 \cdot \left(\frac{\eta \cdot u}{\sigma} \right)^{\frac{1}{6}} \cdot \left(\frac{\eta \cdot u}{\rho_l \cdot g} \right)^{\frac{1}{2}}. \quad (5)$$

For a rotating drum partially immersed in liquid medium, Gelperin et al. [19] suggest

$$s_{adh,min} = 0,94 \cdot \left(\frac{\pi \cdot d \cdot n \cdot \eta}{\sigma} \right)^{\frac{1}{6}} \cdot \left(\frac{3 \cdot n \cdot d \cdot \eta}{4 \cdot \rho_l \cdot g \cdot \left(1 - \frac{\Theta_{dwell}}{360} \right)} \right)^{\frac{1}{2}} \quad (6)$$

for the calculation of the minimum liquid layer at the uppermost part of the drum, where Θ_{dwell} is the immersion angle as shown in Figure 3. This is validated numerically by Hasan and Naser [20]. Both

equations assume backflow of liquid PCM. Thus, the solidification has to be slow compared to the backflow.

2.4 Quasistationary calculation

A first estimation of the heat transfer potential of the rotating drum can be done by the so-called quasistationary approximation, which is described in [21] and [22], among other. Thereby, the thermal capacities of the steel wall and the solidified PCM layer are neglected. Furthermore, the heat transfer from the outer surface of the rotating cylinder towards the ambient air is neglected. The surface-specific heat flux at any point of the submerged drum that has to be transferred from the point of solidification at the boundary of solid and liquid PCM through the solidified PCM and the metal heat exchanger wall to the HTF, can be determined by

$$\dot{q}_1(t) = \frac{1}{\frac{s_{PCM,s}(t)}{k_{PCM,s}} + \frac{1}{K}} \cdot (T_{PCM,m} - T_{HTF}) \quad (7)$$

with

$$\frac{1}{K} = \frac{s_{wall}}{k_{wall}} + \frac{1}{h_{HTF}}. \quad (8)$$

The surface-specific heat flux released by the phase change during solidification of the liquid PCM can be calculated by

$$\dot{q}_2(t) = L_{PCM} \cdot \dot{Q}_{PCM,s} \cdot \frac{ds}{dt} \quad (9)$$

and the surface-specific heat flux resulting from the forced convection due to the overheating of the PCM and the moving surface is given by

$$\dot{q}_3(t) = h_{x,PCM} \cdot (T_{PCM,l} - T_{PCM,m}). \quad (10)$$

The thermal equilibrium at the solidification boundary shown in Figure 4 is

$$\dot{q}_1(t) - \dot{q}_2(t) - \dot{q}_3(t) = 0. \quad (11)$$

By rearranging Equation (11) the thermal equilibrium at the solidification boundary results in

$$\frac{ds}{dt} = \frac{k_{PCM,s} \cdot (T_{PCM,m} - T_{HTF})}{L_{PCM} \cdot \dot{Q}_{PCM,s} \cdot \left(s(t) + \frac{k_{PCM,s}}{K}\right)} - \frac{h_{x,PCM} \cdot (T_{PCM,l} - T_{PCM,m})}{L_{PCM} \cdot \dot{Q}_{PCM,s}}. \quad (12)$$

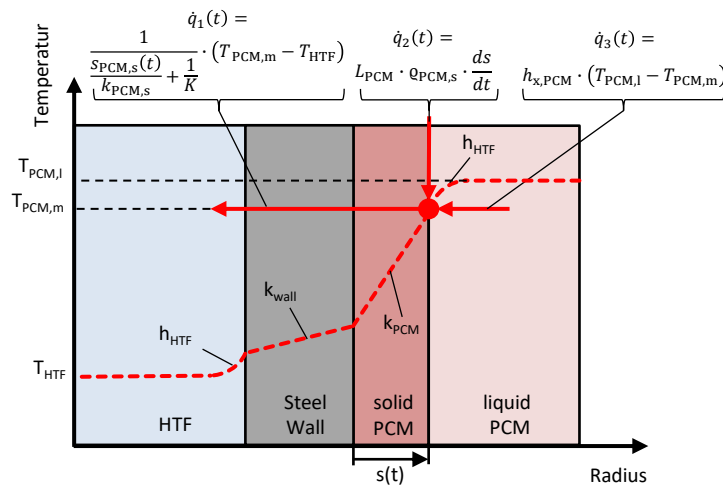


Figure 4: Temperature profile and thermal equilibrium at the solidification point for the quasistationary calculation

The actual total surface-specific heat flux from the point of solidification towards the HTF is

$$\dot{q}_{\text{dwell}}(t) = \dot{q}_1(t) = \dot{q}_2(t) + \dot{q}_3(t) \quad (13)$$

which results in

$$\begin{aligned} \dot{q}_{\text{dwell}}(t) &= L_{\text{PCM}} \cdot \varrho_{\text{PCM},s} \cdot \frac{ds}{dt} + h_{x,\text{PCM}} \cdot (T_{\text{PCM},l} - T_{\text{PCM},m}) \\ &= \frac{1}{\frac{s(t)}{k_{\text{PCM},s}} + \frac{1}{K}} \cdot (T_{\text{PCM},m} - T_{\text{HTF}}) \end{aligned} \quad (14)$$

It is not possible to integrate Equation (12) analytically exactly, but it can be integrated numerically to obtain the time-dependent solidified PCM layer thickness $s_{\text{dwell}}(t)$. In this way, the location-specific HTC $h_{x,\text{PCM}}$ can be implemented as well. The mean surface-specific heat flux of the submerged surface of the drum during the dwell time t_{dwell} can be calculated according to the mean theorem

$$\bar{q}_{\text{dwell}}(t_{\text{dwell}}) = \frac{1}{t_{\text{dwell}}} \int_0^{t_{\text{dwell}}} \dot{q}_{\text{dwell}}(t) \cdot dt \quad (15)$$

by equitation

$$\bar{q}_{\text{dwell}}(t_{\text{dwell}}) = \frac{1}{t_{\text{dwell}}} \sum_0^{t_{\text{dwell}}} \dot{q}_{\text{dwell}}(t) \cdot dt. \quad (16)$$

The dwell time t_{dwell} of a rotating surface element is calculated from the rotational speed n and the submerged angle θ_{dwell} as shown in Figure 3 by

$$t_{\text{dwell}} = \frac{\theta_{\text{dwell}}}{360^\circ} \cdot \frac{1}{n}. \quad (17)$$

The influence of the adhering liquid PCM layer, which solidifies after the surface emerges from the liquid PCM, on the heat transfer can also be estimated by the quasistationary calculation. For this purpose, the thickness of the liquid PCM layer is estimated according to Equation (6) and its temperature is assumed to be the melting temperature of the PCM. Since there is no convective heat transfer anymore, Equation (13) is reduced to

$$\frac{ds}{dt} = \frac{k_{\text{PCM},s} \cdot (T_{\text{PCM},m} - T_{\text{HTF}})}{L_{\text{PCM}} \cdot \varrho_{\text{PCM},s} \cdot \left(s(t) + \frac{k_{\text{PCM},s}}{K} \right)} \quad (18)$$

and the surface-specific heat flux can be calculated by

$$\dot{q}_{\text{adh}}(t) = L_{\text{PCM}} \cdot \varrho_{\text{PCM},s} \cdot \frac{ds}{dt}. \quad (19)$$

The calculation is terminated when the adhesion layer calculated according to Equation (6) has completely solidified. This is given in case

$$s_{\text{adh}}(t) = s_{\text{adh},\text{min}}. \quad (20)$$

In the case that the adhering liquid layer is not completely solidified before it is scraped off, the solidification time is calculated by

$$t_{\text{adh}} = \frac{\theta_{\text{adh}}}{360^\circ} \cdot \frac{1}{n} \quad (21)$$

The average surface-specific heat flux density during the solidification of the adhering liquid is calculated according to Equation (15) by

$$\bar{q}_{\text{adh}}(t_{\text{adh}}) = \frac{1}{t_{\text{adh}}} \sum_0^{t_{\text{adh}}} \dot{q}_{\text{adh}}(t) \cdot dt \quad (22)$$

The average heat transfer for the whole rotating drum is calculated by

$$\bar{q}_{\text{total}} = \bar{q}_{\text{dwell}}(t_{\text{dwell}}) \cdot \frac{t_{\text{dwell}}}{t_{\text{total}}} + \bar{q}_{\text{adh}}(t_{\text{adh}}) \cdot \frac{t_{\text{adh}}}{t_{\text{total}}}. \quad (23)$$

Convective heat transfer from the ambient air to the outer surface of the rotating drum is neglected within the quasistationary calculation. No solidification occurs when the HTF temperature is above the melting point of the PCM. In this case, the surface-specific heat flux is calculated by

$$\dot{q}(t) = \frac{1}{\frac{1}{h_{\text{HTF}}} + \frac{s_{\text{wall}}}{k_{\text{wall}}} + \frac{1}{h_{\text{x,PCM}}}} \cdot (T_{\text{PCM,I}} - T_{\text{HTF}}). \quad (24)$$

2.5 Detailed transient numerical investigation

For a detailed simulation of the heat transfer of the rotating drum, a transient, 1-dimensional numerical scheme has been developed. For this purpose, the heat transfer is investigated by a 1-dimensional section, which is virtually rotated with the rotating drum by time-varying boundary conditions.

For the numerical calculation of a solidification problem, several solutions have been developed in the past. A good overview of several methods can be found in the work of Alexiades and Solomon [23]. For a highly detailed numerical investigation of solidification and melting processes including convection within the liquid phase, the enthalpy-porosity method for the energy equations and a discretization according to the finite-volume method is well known and widely used, e.g. in [24-28]. This method provides excellent results in acceptable simulation time for closed spaces with defined boundary conditions. In addition, a so-called mushy-zone, a region with a certain temperature range where the phase change occurs, can be implemented. Also, the Finite-Element-Method of Galerkin with a varied mesh provides accurate simulation results for solidification and melting behavior of latent heat thermal energy storages as shown e.g. in [29, 30]. Compared to the Finite-Volume-Method, this method has advantages in complex structures due to the adoptable mesh.

The main aim of the numerical scheme developed in this work is to have flexible boundary conditions that can be easily changed several times during the rotation of the drum. Therefore, a Finite-Difference-Method with a varied time step has been chosen, which has been adopted from Baehr and Stephan [22]. Since the time step is varied with each iteration, the choice of the Implicit Euler Scheme for its discretization guarantees stability. The choice of a transient 1-dimensional scheme is sufficient for the simulation of the rotating drum and keeps the simulation simple and the computational times low. Natural convection is not considered in the simulation since forced convection dominates the heat transfer at the rotating drum. A mathematical verification of the numerical simulation is given in Section 0.

2.5.1 Governing equations

The temperature profile from the HTF inside the drum to the liquid PCM or ambient air outside the drum is shown in Figure 5. In Table 1, the governing equations for the different sections are shown. The heat transfer from the HTF inside the drum to the steel wall of the heat exchanger at (1) is reproduced with

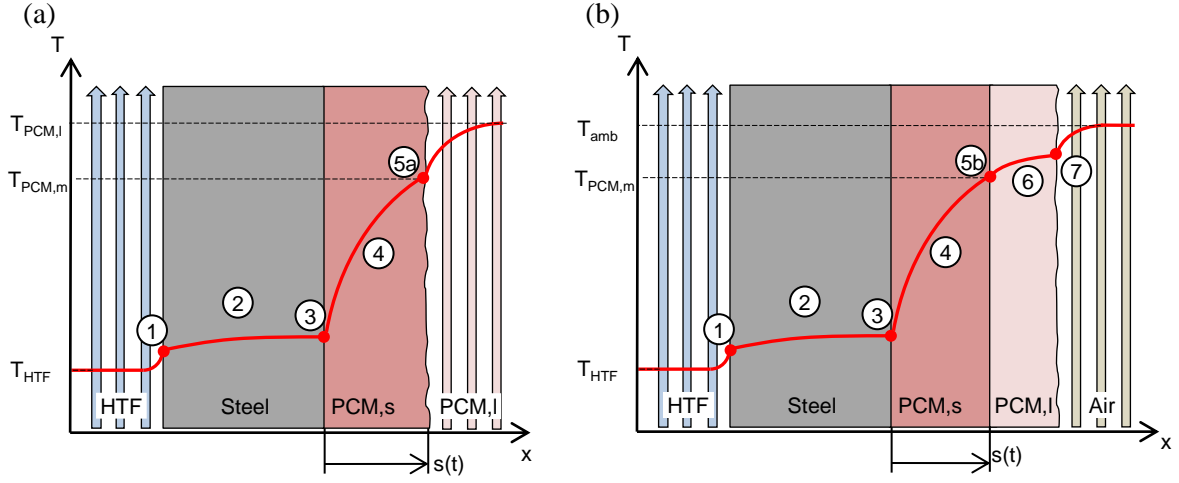


Figure 5: Temperature profile of the heat transfer (a) during the submersion of the drum surface in liquid PCM (b) during the solidification of adhering liquid PCM while the drum surface is rotating in ambient air

convective boundary condition by Equation (25), followed by the partial differential Equation (26) for heat conduction within the steel wall (2). At the boundary between the steel wall and the solidified PCM (3), the specific heat transfer within the solid PCM and the steel must be constant, reproduced by Equation (27). The heat transfer within the solid PCM (4) is also reproduced by the partial differential Equation (28) for heat conduction. At the point of solidification (5), two different cases are considered. In the case of solidification while the surface is immersed in liquid PCM (5a), the local equilibrium is reproduced by Equation (29) analogous to the quasistationary calculation. When adhering liquid PCM is considered while the surface is rotating in ambient air, the equilibrium at the solidification point (5b) is reproduced by Equation (30), which is composed of the heat transferred by conduction within the solidified and liquid adhering PCM and the heat of solidification. The temperature within the adhering liquid PCM (6) is therefore given by Equation (31), another partial differential equation for heat conduction. The heat transfer to the ambient air (7) is given by a convective boundary condition by Equation (32), similar to the heat transfer at the HTF inside the drum.

Table 1: Governing equations for the numerical transient simulation

Location			Equation	
Convective Heat Transfer of HTF	(1)	$x = 0$	$-k_{\text{steel}} \cdot \left(\frac{\partial T}{\partial x} \right)_{x=0} = h_{\text{HTF}} \cdot (T_{\text{wall}} - \vartheta T_{\text{HTF}})$	(25)
Heat conduction steel	(2)	$0 < x < s_{\text{steel}}$	$\frac{\partial T}{\partial t} = a_{\text{steel}} \cdot \frac{\partial^2 T}{\partial x^2}$	(26)
Transfer Steel-PCM _{solid}	(3)	$x = s_{\text{steel}}$	$c_{p,\text{steel}} \cdot \varrho_{\text{steel}} \cdot \frac{\partial T}{\partial t} = \frac{T}{\partial x} \left(k_i \cdot \frac{\partial T}{\partial x} \right)$	(27)
Heat conduction PCM _{solid}	(4)	$s_{\text{steel}} < x < s(t)$	$\frac{\partial T}{\partial t} = a_{\text{PCM},s} \cdot \frac{\partial^2 T}{\partial x^2}$	(28)
Point of Solidification	(5a)	$x = s(t)$	$L_{\text{PCM}} \cdot \varrho_{\text{PCM},s} \cdot \frac{ds}{dt} + h_{x,\text{PCM}} (T_{\text{PCM},l} - T_{\text{PCM},m}) = k_{\text{PCM},s} \cdot \frac{\partial T}{\partial x}$	(29)
	(5b)	$x = s(t)$	$L_{\text{PCM}} \cdot \varrho_{\text{PCM},s} \cdot \frac{ds}{dt} + k_{\text{PCM},l} \cdot \frac{\partial T}{\partial x} = k_{\text{PCM},s} \cdot \frac{\partial T}{\partial x}$	(30)
Heat conduction in adhering liquid	(6)	$s(t) < x < h_{0,\text{min}}$	$\frac{\partial T}{\partial t} = a_{\text{PCM},l} \cdot \frac{\partial^2 T}{\partial x^2}$	(31)

$$\begin{array}{ll} \text{Convective} & \\ \text{Heat Transfer} & (7) \\ \text{of ambient air} & \end{array} \quad x = h_{0,\min} \quad -k_{\text{PCM},l} \cdot \left(\frac{\partial T}{\partial x} \right)_{x=M} = h_{x,\text{amb}} \cdot (T_{\text{PCM},l} - T_{\text{amb}}) \quad (32)$$

2.5.2 Discretization of the equations

The equations shown in Table 1 are discretized by an implicit finite difference method. A varying time step is introduced for consideration of the time-varying solidification rate.

The location-dependent change of temperature is approximated by the symmetric difference quotient of first

$$\frac{\partial T}{\partial x} = \frac{T_{i+1}^k - T_{i-1}^k}{2\Delta x_i} \quad (33)$$

and second order

$$\frac{\partial^2 T}{\partial x^2} = \frac{T_{i-1}^k - 2T_i^k + T_{i+1}^k}{\Delta x_i^2}. \quad (34)$$

The time-dependent change of temperature is approximated by the backward difference quotient

$$\frac{\partial T}{\partial t} = \frac{T_i^k - T_i^{k-1}}{\Delta t}. \quad (35)$$

Thus, the heat conduction within the steel wall (2), the solid PCM (4) and the adhering liquid (6) can be calculated by

$$a_i \frac{T_{i-1}^k - 2T_i^k + T_{i+1}^k}{\Delta x_i^2} = \frac{T_i^k - T_i^{k-1}}{\Delta t}. \quad (36)$$

By introducing

$$r_i = a_i \frac{\Delta t}{\Delta x_i^2} \quad (37)$$

one gets

$$T_i^{k-1} = -r_i \cdot T_{i-1}^k + (1 + 2r_i) \cdot T_i^k - r_i \cdot T_{i+1}^k. \quad (38)$$

Since the geometric thickness of the steel wall is large in compared to the geometric thickness of the solid and adhering PCM layer, the location-depended step Δx_1 within the steel wall can be larger compared to the step-size within the solid and liquid PCM layer Δx_2 to reduce computation time and increase accuracy. Therefore, in the last node of the steel wall $i = s$, Equation (27) is applied and discretized by

$$c_{p,\text{Steel}} \cdot \rho_{\text{steel}} \cdot \frac{T_i^k - T_i^{k-1}}{\Delta t} = k_{\text{PCM},s} \cdot \frac{T_{i+1}^k - T_i^k}{\Delta x_2} - k_{\text{Steel}} \cdot \frac{T_i^k - T_{i-1}^k}{\Delta x_1} \quad (39)$$

what results in

$$T_s^{k-1} = -R \cdot \frac{k_{i+1}}{\Delta x_1 \cdot \Delta x_2} \cdot T_{i+1}^k + \left(R \left(\frac{k_{i+1}}{\Delta x_1 \cdot \Delta x_2} + \frac{k_i}{\Delta x_1^2} \right) + 1 \right) T_i^k - R \cdot \frac{k_i}{\Delta x_1^2} \cdot T_{i-1}^k \quad (40)$$

with

$$R = \frac{\Delta t}{\rho_{\text{Steel}} \cdot c_{p,\text{Steel}}}. \quad (41)$$

Defining the node $i = 1$ as the first node of the steel wall, the convective boundary condition **(1)** can be discretized by

$$T_0^k = T_2^k - \frac{2 \cdot h_{\text{HTF}} \cdot \Delta x_1}{k_{\text{steel}}} (T_1 - T_{\text{HTF}}). \quad (42)$$

When combining (38) and (42), one gets for the first node at $i = 1$

$$T_1^{k-1} + 2 \cdot r_i \cdot Bi_1 \cdot T_{\text{HTF}} = (1 + 2 \cdot r_i \cdot (1 + Bi_1)) \cdot T_1^k - 2 \cdot r_i \cdot T_2^k \quad (43)$$

with

$$Bi_1 = \frac{h_{\text{HTF}} \cdot \Delta x_1}{k_{\text{steel}}} \quad (44)$$

In case of adhering PCM one gets for the last node $i = M$ of the adhering liquid PCM layer accordingly

$$T_M^{k-1} + 2 \cdot r_i \cdot Bi_2 \cdot T_{\text{amb}} = (1 + 2r_i \cdot (1 + Bi_2)) \cdot T_1^k - 2 \cdot r_i \cdot T_2^k \quad (45)$$

with

$$Bi_2 = \frac{h_{\text{x,amb}} \cdot \Delta x_2}{k_{\text{PCM,s}}}. \quad (46)$$

The point of solidification at node $i = n$ is assumed to be an isothermal wall with the temperature of the melting point of the PCM. Therefore, Equation (38) for the node $i = n-1$ is adapted to

$$T_{n-1}^{k-1} + r_i T_n^k = -r_i \cdot T_{n-2}^k + (1 + 2r_i) \cdot T_{n-1}^k \quad (47)$$

and in case of adhering liquid PCM the node $i=n+1$ is adapted accordingly to

$$T_{n+1}^{k-1} + r_i T_n^k = -r_i \cdot T_{n+2}^k + (1 + 2r_i) \cdot T_{n+1}^k \quad (48)$$

with

$$T_n^k = T_n^{k-1} = T_m. \quad (49)$$

To reproduce the solidification, the isothermal boundary condition at $i = n$ is moving within the mesh with every iteration step. The time of an iteration step Δt is calculated from Equation (29) in case of solidification within the liquid PCM by

$$\Delta t = \frac{h_{\text{PCM}} \cdot \rho \cdot \Delta x}{k_{\text{PCM,s}} \cdot \frac{T_n^{k-1} - T_{n-1}^{k-1}}{\Delta x_2} - h_{\text{x,PCM}} \cdot (T_{\text{PCM,l}} - T_{\text{PCM,m}})} \quad (50)$$

and in case of adhering liquid PCM by

$$\Delta t = \frac{h_{\text{PCM}} \cdot \rho \cdot \Delta x}{k_{\text{PCM,s}} \cdot \frac{T_n^{k-1} - T_{n-1}^{k-1}}{\Delta x_2} - k_{\text{PCM,l}} \cdot \frac{T_{n+1}^{k-1} - T_n^{k-1}}{\Delta x_2}}. \quad (51)$$

Equation (38), (40), (43), (45), (47) and (48) results in a system of linear dependent equations. They can be summarized by

$$\bar{\mathbf{M}}^k \cdot \vec{\mathbf{T}}^k = \vec{\mathbf{T}}^{k-1} + \vec{\mathbf{b}}$$

with the vectors of the temperature in the previous \vec{T}^{k-1} and current \vec{T}^k time step, the boundary conditions within vector \vec{b} and a sparse band matrix $\bar{\bar{M}}^k$. The Matlab® routine mldivide is used for solving the linear system.

2.6 Material Properties

For the validation of the introduced models the experimental data published in [1] are used. Therefore, the material properties of decanoic acid are required which are given in Table 2. An analysis of the sensitivity of the materials properties, discussed in section 3.5, shows that the density of the solid phase, the phase change enthalpy, the thermal conductivity of the PCM and the viscosity of the liquid PCM have an important influence of both, the transferred heat as well as the thickness of the solidified PCM layer. Therefore, these properties are measured within this research. The phase change enthalpy is measured by differential scanning colometry, the thermal conductivity is measured by a parallel-plate thermal conductivity apparatus, the density is determined by measuring the displacement of water and the viscosity is measured by a rheometer. The results are given in Table 2 as well. For the calculation and discussion of a high temperature heat exchanger for latent heat storage using sodium nitrate as PCM, the material properties given in Table 3 are used. As the material properties closely to their melting temperature influences the calculation the most, the temperature dependence of the materials is neglected and values close to the melting point are selected.

Table 2: Thermophysical properties of decanoic acid

Description	Variable	Value	Unit	Remark	Source
Melting point	$T_{PCM,m}$	31.5	°C		[31]
Phase change enthalpy	L_{PCM}	164.1	kJ·kg ⁻¹		measured
Thermal conductivity, liquid	$k_{PCM,l}$	0.149	W·m ⁻¹ ·K ⁻¹	(at 40 °C)	[31]
Thermal conductivity, solid	$k_{PCM,s}$	0.1763	W·m ⁻¹ ·K ⁻¹	(at 17.5 °C)	measured
Density, liquid	$\rho_{PCM,l}$	886.3	kg·m ⁻³	(at 37.8 °C)	[32]
Density, solid	$\rho_{PCM,s}$	916	kg·m ⁻³	(at 21 °C)	measured
Viscosity	$\eta_{PCM,l}$	0.0073	Pa·s	(at 34 °C)	measured
Heat capacity, liquid	$c_{p,PCM,l}$	2.0883	kJ·kg ⁻¹ ·K ⁻¹	(at 35-65 °C)	[33]
Heat capacity, solid	$c_{p,PCM,s}$	2.0967	kJ·kg ⁻¹ ·K ⁻¹	(at 0-24 °C)	[33]
Surface tension	$\sigma_{PCM,l}$	0.0277	N·m ⁻¹	(at 31.9 °C)	[34]

Table 3: Thermophysical properties of sodium nitrate

Description	Variable	Value	Unit	Remark	Source
Melting point	$T_{PCM,m}$	306	°C		[3]
Phase change enthalpy	L_{PCM}	178	kJ·kg ⁻¹		[3]
Thermal conductivity, liquid	$k_{PCM,l}$	0.514	W·m ⁻¹ ·K ⁻¹	at 317 °C	[35]
Thermal conductivity, solid	$k_{PCM,s}$	0.73	W·m ⁻¹ ·K ⁻¹	at 246 °C	[3]
Density, liquid	$\rho_{PCM,l}$	1908	kg·m ⁻³	at 306 °C	[36]
Density, solid	$\rho_{PCM,s}$	2113	kg·m ⁻³	at 306 °C	[36]
Viscosity	$\eta_{PCM,l}$	0.002854	Pa·s	at 317 °C	[37]
Heat capacity, liquid	$c_{p,PCM,l}$	1.655	kJ·kg ⁻¹ ·K ⁻¹	at 306 °C	[3]
Heat capacity, solid	$c_{p,PCM,s}$	1.384	kJ·kg ⁻¹ ·K ⁻¹	at 150 °C	[3]
Surface tension	$\sigma_{PCM,l}$	0.1196	N·m ⁻¹	at 316 °C	[38]

2.7 Verification of the models

There is no analytically exact solution for the calculation of the given solidification problem. Therefore, the mathematical problem is reduced to certain boundary conditions for verification. The analytical solution of Stefan, first presented in [39] and described in detail in [22], can be used to verify the numerical scheme and the quasistationary calculation when reducing the problem to solidification of a liquid PCM at melting temperature on an isothermal wall with a temperature below the melting temperature. The Neumann-Solution described in [40] is used for the verification of the solidification process of the adherent liquid after the surface is removed from the PCM-tub. Again, convective heat transfer inside the drum and heat conduction inside the steel wall are neglected to assume an isothermal solidification wall. The time-dependent heat transferred at the isothermal wall and the thickness of the solidified PCM layer are given in Figure 4. The assumed temperature difference between the isothermal wall and the melting temperature of the PCM is 10 K for decanoic acid and 100 K for sodium nitrate in the Stefan-Solution. For the Neumann-Solution, an additional temperature difference between the melting point and the liquid PCM of 10 K for decanoic acid and 100 K for sodium nitrate is assumed, resulting in a total temperature difference of 20 K and 200 K, respectively. The difference in solidified layer thickness and transferred heat between the numerical solutions and the exact solutions is less than 0.05 %, which verifies the numerical simulation. The quasistationary solution overestimates both the layer thickness and the heat transfer, and the deviations of the calculated layer thickness and heat transfer are equal in percentage. The deviation is 2 % for the calculation with decanoic acid and 11 % for the calculation with sodium nitrate. In the case of complete heat transfer from the inner HTF to the liquid PCM with a temperature above the melting point of the PCM and a constant outer convective heat transfer coefficient, the thickness of the solidified PCM layer and the heat flux takes constant values when viewed for a long period of time. In this case, the steady-state solutions of the numerical simulation and the quasistationary calculations must be identical after a long period of time, which is the case for the presented numerical model. For an estimation of the error due to the use of axial coordinates instead of cylindrical coordinates, no analytically exact solutions could be identified by the authors. For radial coordinates, analytically exact solutions are identified only for point and line heat sources, which are not applicable to the current problem. When reducing the problem to a solidification process on an isothermal wall, the ratio between the radius of the inner isothermal wall and the radius of the outer solidification front is 0.989, assuming a layer thickness of 1 mm. Since this ratio is close to 1, corresponding to a flat wall, the influence of the axial coordinates can be neglected. The overall ratio

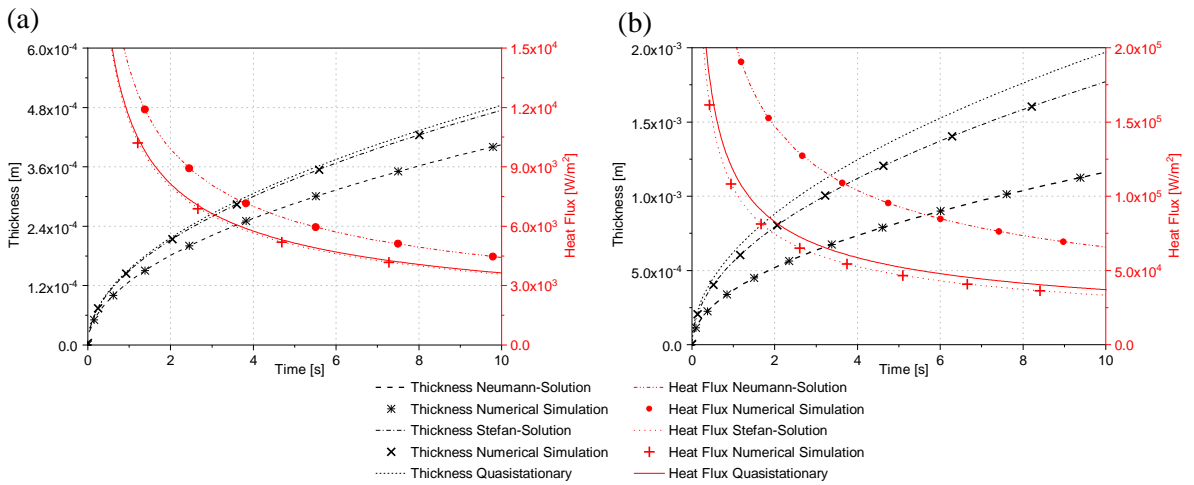


Figure 6: Verification of the models (a) for decanoic acid with a temperature difference of 10 K between the HTF and the melting point and further 10 K between the melting point and liquid PCM (b) for sodium nitrate with a temperature difference of 100 K between the HTF and the melting point and further 100 K between the melting point and liquid PCM

between the inner radius passed by the HTF and the outer radius where solidification occurs is 0.935, assuming a layer thickness of the solidified PCM of 1 mm. Here, the error due to the use of axial coordinates instead of cylindrical coordinates can be estimated by comparing the presented quasistationary solution with the quasistationary solution using cylindrical coordinates, also presented in [22]. The deviation of both, the solidified layer thickness as well as the heat flux is below 1 % at rotational speeds below 4 min^{-1} and is rising up to 4 % at 35 min^{-1} .

3 Comparison of the models with experimental data

In this section, the data calculated with the introduced models are compared with the experimental data from [1] and later discussed in section 3.5. Both temperature differences, the difference between the temperature of the HTF inside the rotating drum and the melting point of the PCM ($T_{m,PCM} - T_{HTF}$) and the temperature difference between the melting point of the PCM and the temperature of the liquid PCM ($T_{l,PCM} - T_{m,PCM}$) affect the heat transfer. These both temperature differences are also illustrated in Figure 4 and Figure 5(a). The temperature setting of the presented data are given together with the total temperature difference between the temperature of the HTF and the temperature of the liquid PCM as shown in Figure 7.

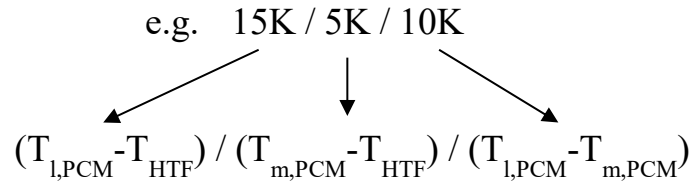


Figure 7: Nomenclature of the temperature setting

3.1 Thickness of the adhering layer

The thickness of the adhesive layer given in [1] is calculated from the measured layer thicknesses with and without adhesion. At rotational speeds above 12 min^{-1} , the measured adhesive layer was not completely solidified when scraped off the drum and was therefore not measured in detail. Therefore, only values up to 12 min^{-1} are compared. The calculation according to Landau-Levich (Equation (5)) overestimates the adhesion layer thickness by 139 % on average. If the measured values are compared with the values calculated according to Gelperin (Equation (6)), the average deviation is 39 %.

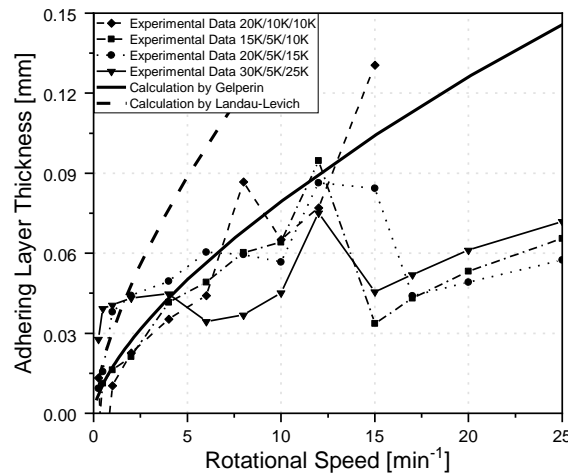


Figure 8: Measured and calculated adhesion layer thicknesses

3.2 Convective heat transfer without solidification

In case of a HTF temperature inside the rotating drum above the melting temperature of the PCM, no solidification occurs. Convection of the liquid PCM on the rotating drum wall is dominates the heat transfer in this case. Figure 9 compares the measured heat transfer without adhesion with the calculated heat transfers of the numerical simulation and the quasistationary calculation. While the quasistationary calculation underestimates the heat transfer by 37 % on average, the numerical simulation reproduces the measured values above a rotational speed of 4 min^{-1} with an underestimation of 8 % on average. At low rotational speeds below 4 min^{-1} , the experimental values exceed the numerically calculated values by 36 % on average. When adhering liquid PCM is included, the increase in the heat transfer at increasing rotational speeds is more linear compared to the values without adhesion. This is also reproduced by the numerical simulation shown in Figure 10. While the numerical simulation reproduces the measured value for rotational speeds above 4 min^{-1} with an average deviation of 11 %, the measured values below 4 min^{-1} are underestimated by 31 % on average. No quasistationary calculations are available for the case of convective heat transfer with adhesion, since the heat capacity of the adhering liquid PCM layer is neglected by the quasistationary calculation.

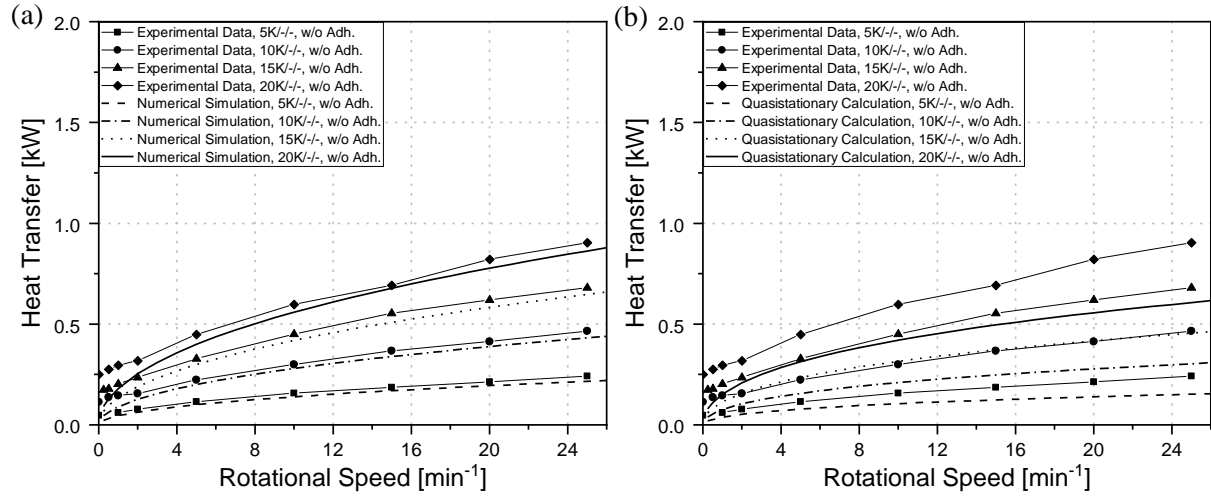


Figure 9: Comparison of the measured convective heat transfer without solidification and without adhesion at the rotating drum (a) with the numerical simulation (b) with the quasistationary calculation

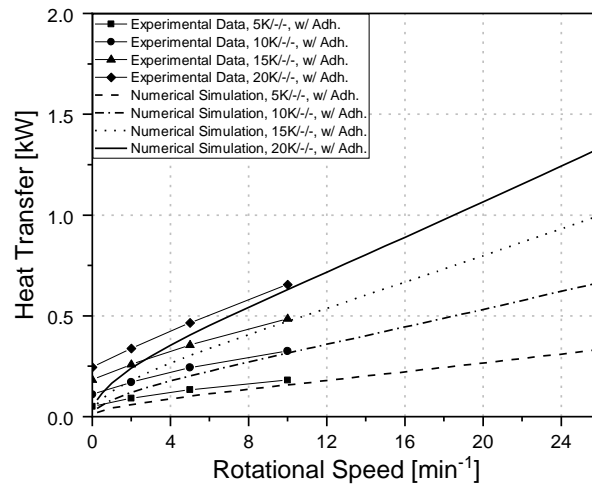


Figure 10: Comparison of the measured convective heat transfer without solidification with adhesion at the rotating drum with the numerical simulation

3.3 Heat transfer with solidification

If the adhering liquid layer is removed by a rubber lip shortly after the surface emerges from the liquid PCM, the solidification of the PCM is limited to the immersed surface only. The convective heat transfer from the outer solidified PCM layer to the ambient air is only considered in the numerical simulation, but neglected in the quasistationary calculation. Figure 11 compares the experimental data with the calculated values. The quasistationary calculation underestimates the experimental data by 30 % on average. Focusing on the values with a temperature difference of 5 K between the temperature of the HTF inside the drum and the melting temperature of the PCM, it is noticeable that the increase in heat flux due to an increase in the temperature difference between the melting temperature of the PCM and the temperature of the liquid PCM is similar in absolute values. The numerical simulation reproduces the experimental data on average with a deviation of 17 %. While the deviation for the temperature setting of 15K/5K/10K is below 15 %, the numerical simulation underestimates the experimental values of the temperature setting of 20K/10K/10K by 18 % on average. Similar to purely convective heat transfer, the simulation reproduces the heat transfer at rotational speeds above 4 min^{-1} with a deviation of 11 %, while the deviation is 22 % on average at rotational speeds below 4 min^{-1} .

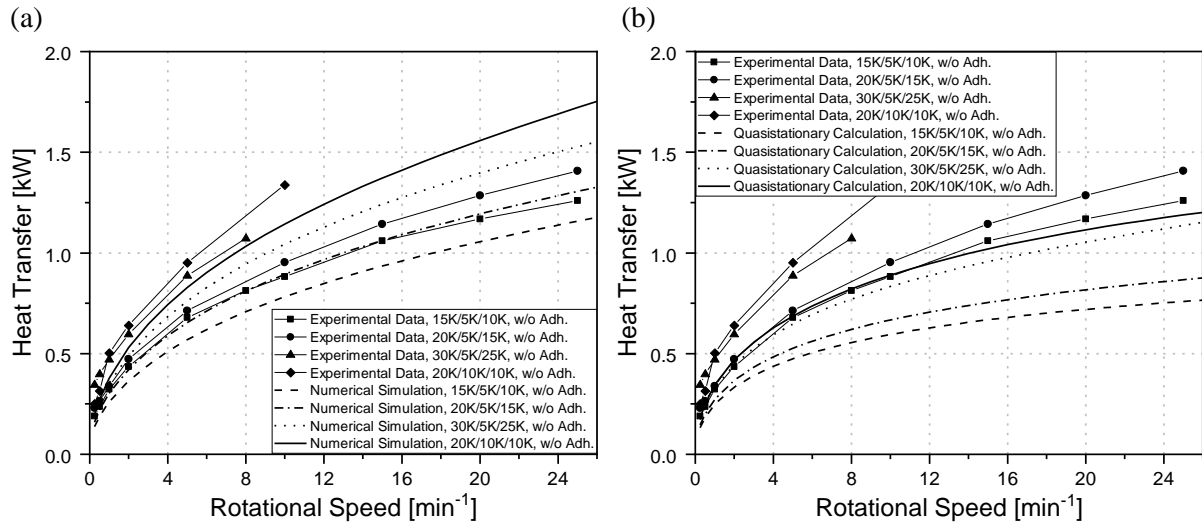


Figure 11: Comparison of the measured heat transfer during solidification and without adhesion at the rotating drum (a) with the numerical simulation (b) with the quasistationary calculation

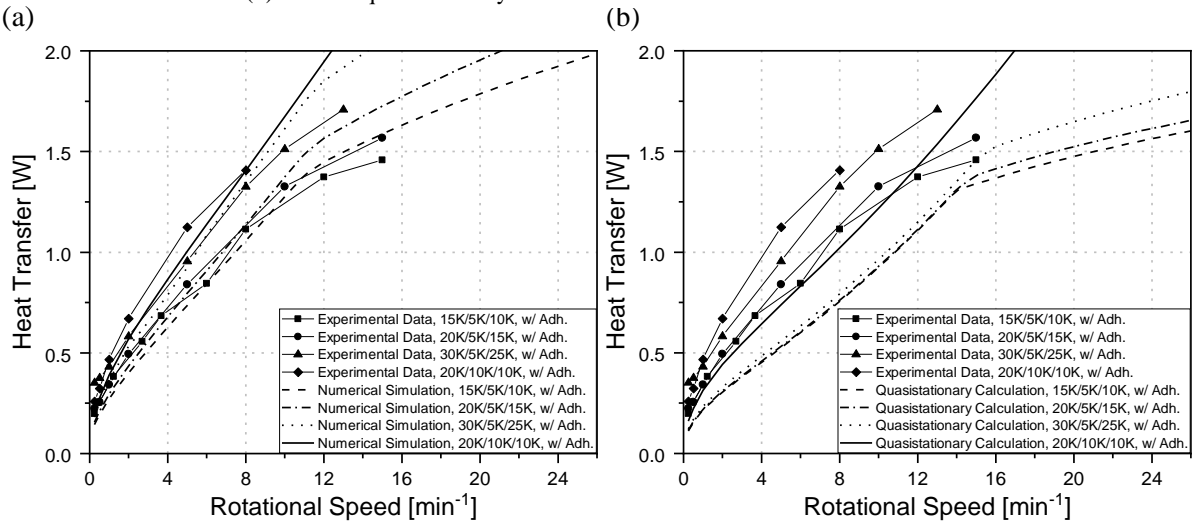


Figure 12: Comparison of the measured heat transfer during solidification with adhesion at the rotating drum (a) with the numerical simulation (b) with the quasistationary calculation

If the adhering layer of liquid PCM is not removed by a rubber lip, the adhering layer of liquid PCM solidify after the surface has left the liquid PCM. This increases the surface where solidification takes place and thus increases the effective heat flux. Figure 12 shows the calculated and the experimental data. The data of the numerical simulation and the quasistationary calculation show an almost linear growth of the heat flux with increasing rotational speeds up to a significant point where the growth flattens out. At this point, the adhering layer is not yet fully solidified when it reaches the scraper. At a temperature difference of 5 K between the temperature of the HTF and the melting point of the PCM the point of flattening calculated by the numerical simulation is at a rotational speed of 11 min^{-1} , while the quasistationary calculation determinates the point of flattening at 14 min^{-1} . The point of flattening is more significant in the data of the quasistationary calculation. For the temperature configuration 20K/10K/10K, the point of flattening is above the range shown. The quasistationary calculation underestimates the experimental data by 37 % on average. Contrary to the results of the heat flux without adhesion, the increase of the heat flux due to the increase of the temperature of the liquid PCM is not reproduced by the quasistationary calculation. The numerical simulation reproduces the experimental data with an accuracy of 14 % on average. Again, the deviation is 6 % on average at rotational speeds above 4 min^{-1} while the deviation is 20 % for rotational speeds below 4 min^{-1} .

3.4 Thicknesses of the solidified PCM layer

The calculation methods presented can also be used to calculate the solidified layer thickness at the rotating drum. The results of the calculations are compared with the measured values in Figure 13 for the case with adhesion and in Figure 14 for the case without adhesion. The layer thickness is reproduced qualitatively correct by both calculation approaches. In the case of adhering liquid PCM, as already mentioned in section 3.1, the layer was not completely solidified when reaching the scraper at high rotational speeds. This can be seen in the experimental data and is also reproduced by the models. At a temperature difference of 5 K between the HTF and the melting point of the PCM, the significant bend in the layer thickness is found in the experimental data at a rotational speed of 12 min^{-1} , which is reproduced by the transient numerical simulation correctly. The data calculated by the quasistationary approach shows this bend at a rotational speed of 16 min^{-1} . In case of a temperature difference of 10 K between the HTF and the melting temperature of the PCM, the experimentally measured layer thickness is reproduced by the transient numerical simulation with a deviation of 6 % on average and is underestimated by the quasistationary calculation by 12 % on average. The experimentally measured layer thickness at a temperature difference of 5 K between the HTF and the melting temperature of the PCM is underestimated by both calculation methods. While the transient numerical simulation underestimates the measured values by 110 % on average, the quasistationary calculation underestimates the measured values by 71 % on average. The deviation of the calculation from the experimental data is higher with an increased temperature difference between the melting temperature of the PCM and the temperature of the liquid PCM. Thus, the average deviation of the calculated data obtained by the numerical simulation is increased from 59 % to 178 % when the temperature difference between the melting temperature of the PCM and the temperature of the liquid PCM is increased from 10 K to 25 K, with a common temperature difference of 5 K between the HTF and the melting point of the PCM.

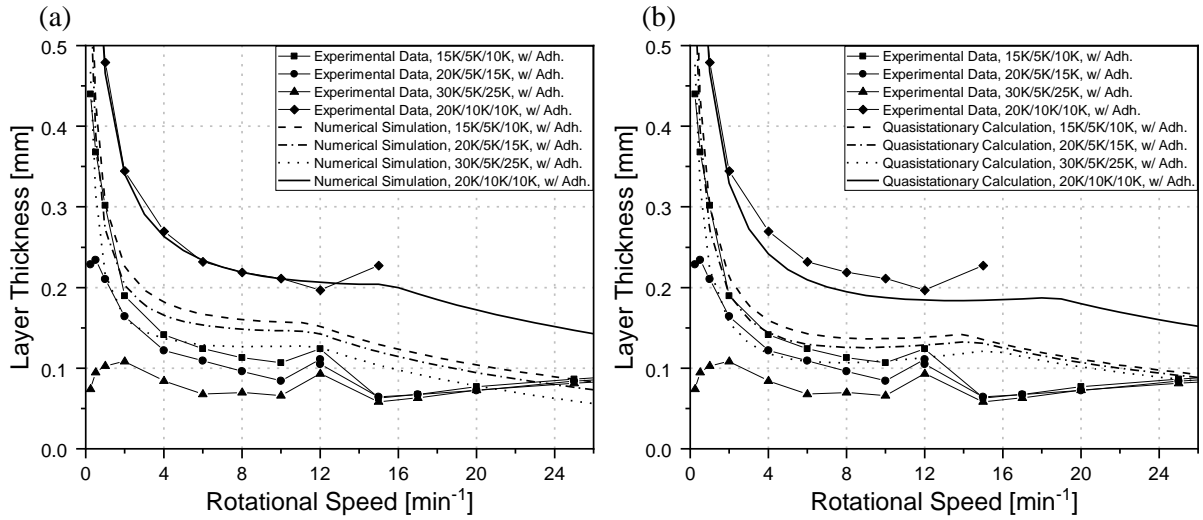


Figure 13: Comparison of the measured layer thicknesses with adhesion at the rotating drum (a) with the numerical simulation (b) with the Quasi-Steady calculation

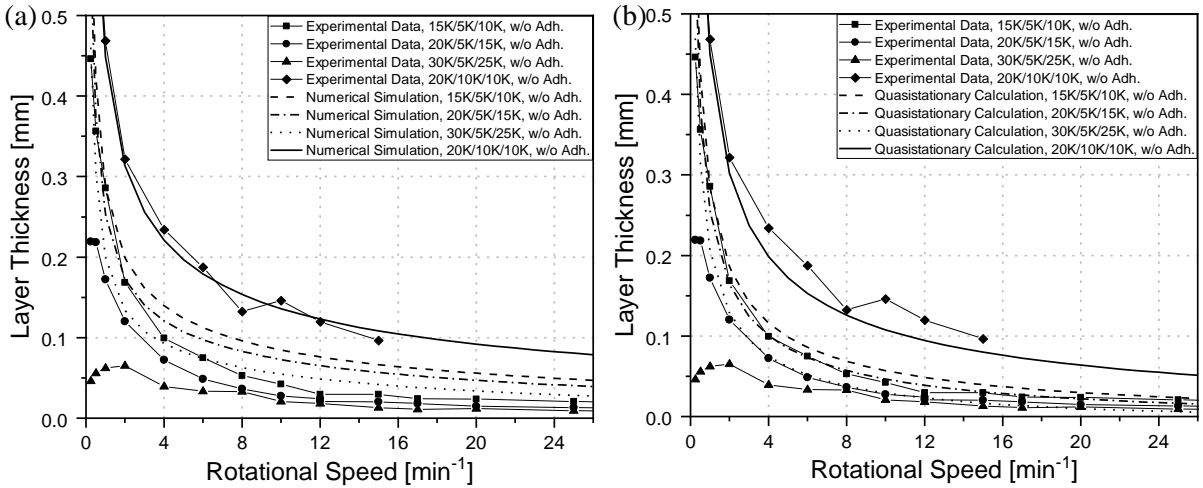


Figure 14: Comparison of the measured layer thicknesses without adhesion at the rotating drum (a) with the numerical simulation (b) with the Quasi-Steady calculation

3.5 Discussion of the deviations and the influence of the material properties

When comparing the deviation of the heat flux calculated by the quasistationary calculation and the transient numerical simulation, the results of the quasistationary calculation are always and on average 22 % lower instead of the data calculated by the numerical simulation. Since the quasistationary calculation shows a slightly increased heat flux of 2 % on average in the verification (Section 0), this may be unexpected. To explain this behaviour, the unsteady effects during the rotation of the one-dimensional solidification line have to be considered. So, the solidified layer grows when immersed in liquid PCM, while the temperature inside the solidified PCM layer and the steel wall is almost constant due to the isothermal solidification front. The same behaviour continues when adhering PCM solidifies but the temperature of the liquid adhering layer decreases. When the adhesion layer is completely solidified, the temperature inside the steel wall and the solidified PCM layer decreases since there is still a temperature difference to the temperature of the inner HTF. This is also continued within the steel wall after the solidified PCM layer is scraped off. At the point of immersion, the steel wall heats up, resulting in increased heat transfer and an increased growth rate of the PCM layer.

The results of the calculation of the adhesive layer thickness presented in Section 3.1 show that the backflow of liquid adherent PCM has to be considered, which agrees with visual observations during

the experiments. Contrary to this, the simulation tool assumes a constant thickness of the adhesion layer thickness in which only heat conduction is considered. Since the backflow of the adhering liquid PCM is only gravimetrically driven and therefore assumed to be laminar, the assumption of radial heat conduction is correct in a first approximation. Nevertheless, the thickness of the adhering liquid PCM layer is underestimated on average by the numerical simulation. This results in faster cool-out of the adhering layer, which can be a reason for the overestimation of the solidified layer thickness in the numerical simulation. The change of the boundary condition at the point of emersion leads to a slight local reduction of the solidified layer thickness due to melting. While a convective boundary condition is assumed within the liquid PCM, this is immediately changed to adhering liquid PCM with uniform temperature at the point of emersion. At this moment, the high temperature gradient at the solidification point leads to a reduction of the layer thickness, followed by further solidification after the adhering liquid PCM layer is cooled down.

For rotational speeds below 2 min^{-1} , the numerical simulation underestimates the experimental data of the heat transfer more compared to higher rotational speeds. In the same way, the layer thickness determinate by the numerical simulation overestimates the experimental data in this range. This is assumed to be an effect of natural convection within the liquid PCM, which exceeds the forced convection at these rotational speeds. Natural convection is not considered in the current models. The research shows the limitations of neglecting natural convection, which becomes dominant for low rotational speeds. The experimental data of fully immersed rotating cylinders given in [8] supports this assumption.

The heat transfer and layer thicknesses are affected by several geometrical and material-specific properties. Especially the material-specific properties of the PCM used are essential and difficult to determine due to the proximity of the melting point. Figure 15 shows the effect of a change in key properties on heat transfer and the layer thickness. One can see a high influence of the density and the phase change enthalpy of the PCM, followed by the thermal conductivity and the viscosity of the PCM. The temperatures of the rotating drum, namely the temperature of the HTF, the melting temperature of the PCM, the ambient temperature and the temperature of the liquid PCM, also have an influence on the

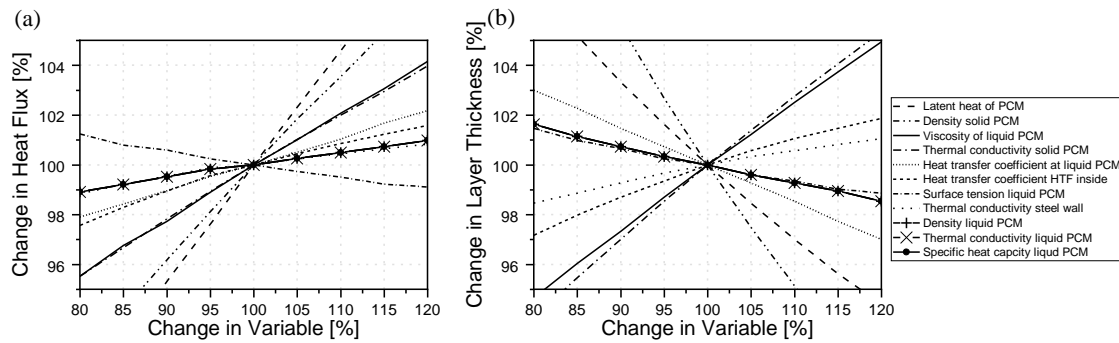


Figure 15: Sensitivity of the material properties and heat transfer coefficients (a) on the heat flux (b) on the layer thickness

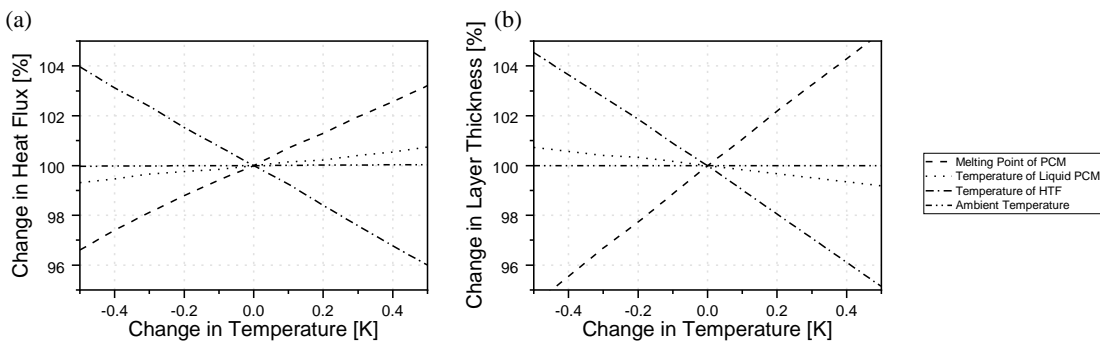


Figure 16: Sensitivity of the temperatures (a) on the heat flux (b) on the layer thickness

heat transfer and the layer thickness. The influence of a change in these temperatures is shown correspondingly in Figure 16. A change in the ambient temperature and the temperature of the liquid PCM has comparatively little effect on the heat transfer and the layer thickness, while the influence of a change in the HTF temperature and the melting point of the PCM is much higher. For the melting temperature, which is considered to be 31.5 °C in this work, values between 30.1 °C [41] and 32.15°C [42] can be identified in the literature. Furthermore, both calculation tools introduced assume a sharp melting point without supercooling.

4 Potential of the rotating drum heat exchanger using a high-temperature PCM

With the introduced numerical simulation, a heat exchanger based on the rotating drum can be calculated for the generation of steam. Thereby, sodium nitrate (NaNO_3), whose melting point is 306°C, is assumed to be the PCM, while the geometrical properties of the rotating drum presented in [1] remain unchanged. The evaporation of the HTF inside the drum significantly increases the internal surface-specific heat transfer coefficient as mentioned in Section 2.2. The use of a high temperature PCM allows an increased temperature difference between both the melting point of the PCM and the evaporating HTF and between the melting point of the PCM and the liquid PCM. The resulting surface-specific heat flux based on the entire surface of the drum is shown in Figure 17. It is increased for higher temperature differences and for higher rotational speeds and is exceeding 400 $\text{kW}\cdot\text{m}^{-2}$ for a total temperature difference of 160 K and a rotational speed of 150 min^{-1} . For a comparison of the heat transfer potential of different heat transfer techniques, the coefficient of heat transfer in $\text{W}\cdot\text{m}^{-2}\cdot\text{K}^{-1}$ is given in Figure 18. The coefficient of heat transfer is strongly nonlinear for different rotational speeds and temperature differences. The nonlinear behavior is mainly based on the nonlinearity of the solidification process. At low temperature differences the coefficient of heat transfer is highest reaching values higher than 5000 $\text{W}\cdot\text{m}^{-2}\cdot\text{K}^{-1}$. With increasing temperature difference, the coefficient of heat transfer decreases regressively. At a temperature difference of 150 K, the coefficient of heat transfer is still exceeding 3000 $\text{W}\cdot\text{m}^{-2}\cdot\text{K}^{-1}$. Compared to values of typical evaporators, which range from 900 $\text{W}\cdot\text{m}^{-2}\cdot\text{K}^{-1}$ to 3000 $\text{W}\cdot\text{m}^{-2}\cdot\text{K}^{-1}$ [43], the rotating drum is competitive, considering that the authors of the study did not perform any optimization with respect to the geometrical characteristics and the design of the rotating drum within the scope of this study. While the high surface-specific heat fluxes at increased temperature differences are well suited for the generation of process steam with high power density, the high coefficients of heat transfer at low temperature differences illustrates the high potential for exergetically efficient heat transfer.

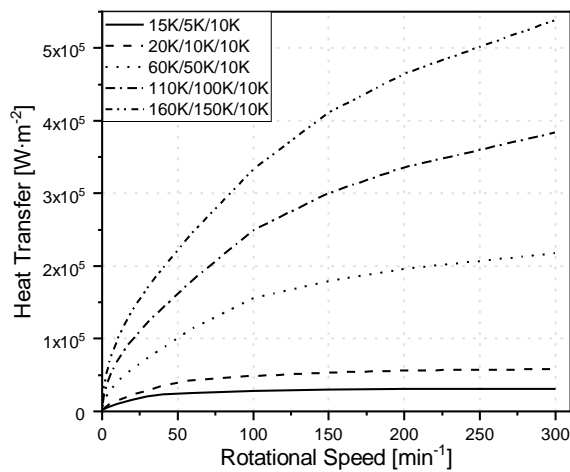


Figure 17: Heat transfer from the liquid PCM to the HTF at the rotating drum

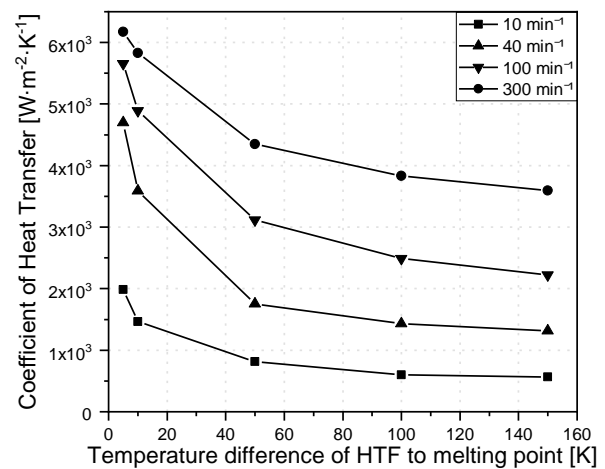


Figure 18: Total heat transfer coefficient from the liquid PCM to the HTC at the rotating drum

5 Summary and Outlook

With the rotating drum heat exchanger, thermal energy from latent heat as well as thermal energy from sensible heat can be transferred with high surface-specific heat flux densities. Thereby, a horizontally rotating drum is partially immersed in liquid PCM while a HTF passing through the drum is heated up. At a HTF temperature below the melting point of the PCM, the PCM is solidified on the outer side of the rotating drum. In this case, the solidified PCM layer is removed by a fixed scraper with each rotation. At a HTF temperature above the melting point of the PCM, no solidification occurs and the heat transfer is based on forced convection only. In both cases, liquid PCM adheres to the surface when it is released from the tub, which increases the effective heat transfer surface.

Within this research, two novel calculation approaches for the calculation of the heat transfer as well as the layer thickness of the rotating drum heat exchanger are introduced, with the objective of obtaining a calculation tool for large-scale high-temperature rotating drum heat exchanger for latent heat storage. The first is based on the quasistationary solution of the Stefan-problem. The second is a transient numerical simulation based on the Finite-Differences-Method. For both calculation approaches, a surface coefficient of heat transfer on the outer side of the rotating drum is required. Since this heat transfer problem is similar to a moving surface in a quiescent medium, the correlation of Tsou could be identified, which is also verified for partially immersed cylinders. For the thickness of the liquid PCM adhering to the solidified surface after the drum surfaces emerge from the liquid PCM, a calculation of Landau and Levich could be identified.

The calculation approaches are verified by mathematically exact solutions. For the validation of the calculations, experimental data are available for a temperature difference of up to 10 K between the HTF inside the rotating drum and the melting point of the PCM, and a temperature difference of up to 25 K between the melting point of the PCM and the liquid PCM. The experiments were performed in previously published research on a rotating drum with a diameter of 184 mm at rotational speeds of up to 25 min^{-1} using decanoic acid with a melting temperature of 31.5 K as PCM.

The transferred heat can be calculated qualitatively correctly with both calculation approaches in the case of solidification and in the case of no solidification. Thereby, the transferred heat increases with higher rotational speeds. Furthermore, adhering PCM increases the heat transfer. In case of no solidification, the heat transfer through the heat exchanger wall is mainly affected by the surface coefficient of heat transfer on the outer surface of the rotating drum. When solidification occurs, the released phase change enthalpy of the solidifying PCM affects the heat transfer the most. But also, increasing the external surface coefficient of heat transfer between the moving solidified PCM layer and the liquid PCM increases the heat transfer, while the thickness of the solidified PCM layer decreases in this case. The research shows that the correlation of the surface coefficient of heat transfer of the outer surface identified for no solidification might also be valid in the case of simultaneous solidification. The quasistationary calculation underestimates the heat transfer on average by 37 % in case of no solidification and 33 % in case of solidification and is therefore only suitable for a rough calculation of a rotating drum heat exchanger. The transient numerical simulation reproduces the heat transfer on average with an accuracy of 9 % in case of no solidification and 8 % in case of solidification at rotational speeds above 4 min^{-1} . For rotational speeds below 4 min^{-1} , the numerical simulation underestimates the experimental data by 24 % on average. For an accurate calculation at low rotational speeds, natural convection has to be included into the model.

Assuming NaNO_3 as PCM with a temperature difference of 150 K between an evaporating HTF inside the rotating drum and the melting point of the PCM, a surface-specific heat flux density of up to $500 \text{ kW}\cdot\text{m}^{-2}$ for a rotational speed of 300 min^{-1} can be assumed based on the numerical simulation.

In a next step, the numerical tool will be used for the identification of an optimized design of the rotating drum heat exchanger for latent heat thermal energy storage in an industrial-scale application. For the validation of the numerical simulation of a high-temperature system, an experimental test rig using a high-temperature PCM and direct evaporation within the rotating drum is in planning.

CRedit authorship contribution statement

Jonas Tombrink: Conceptualization, Methodology, Investigation, Validation, Visualization, Writing - original draft. Dan Bauer: Conceptualization, Funding acquisition, Supervision, Writing - review & editing.

Declaration of Competing Interest

The authors declare that they have no known competing financial interests or personal relationships that could have appeared to influence the work reported in this paper.

Funding

This research did not receive any specific grant from funding agencies in the public, commercial, or not-for-profit sectors.

6 References

- [1] J. Tombrink, H. Jockenhöfer, D. Bauer, Experimental investigation of a rotating drum heat exchanger for latent heat storage, *Appl. Therm. Eng.*, 183 (2021) 116221. <https://doi.org/10.1016/j.applthermaleng.2020.116221>
- [2] J. Tombrink, H. Jockenhöfer, D. Bauer, Examination of the heat transfer potential of an active latent heat storage concept, in: *Eurotherm Seminar n°112 - Advances in Thermal Energy Storage*, Lleida, Spain, 2019.
- [3] T. Bauer, D. Laing, R. Tamme, Characterization of Sodium Nitrate as Phase Change Material, *Int. J. Thermophys.*, 33 (2012) 91-104. <https://doi.org/10.1007/s10765-011-1113-9>
- [4] W.D. Steinmann, The CHEST (Compressed Heat Energy STORAGE) concept for facility scale thermo mechanical energy storage, *Energy*, 69 (2014) 543-552. <https://doi.org/10.1016/j.energy.2014.03.049>
- [5] H. Jockenhöfer, W.-D. Steinmann, D. Bauer, Detailed numerical investigation of a pumped thermal energy storage with low temperature heat integration, *Energy*, 145 (2018) 665-676. <https://doi.org/10.1016/j.energy.2017.12.087>
- [6] T. Naegler, S. Simon, M. Klein, H.C. Gils, Quantification of the European industrial heat demand by branch and temperature level, *Int. J. Energ. Res.*, 39 (2015) 2019-2030. <https://doi.org/10.1002/er.3436>
- [7] M. Rehfeldt, T. Fleiter, F. Toro, A bottom-up estimation of the heating and cooling demand in European industry, *Energy Effic.*, 11 (2017) 1057-1082. <https://doi.org/10.1007/s12053-017-9571-y>
- [8] J.T. Anderson, O.A. Saunders, Convection from an isolated heated horizontal cylinder rotating about its axis, *Proc. R. Soc. Lond. A*, 217 (1953) 555-562. <https://doi.org/10.1098/rspa.1953.0080>
- [9] B. Özerdem, Measurement of convective heat transfer coefficient for a horizontal cylinder rotating in quiescent air, *Int. Commun. Heat. Mass. Transf.*, 27 (2000) 389-395. [https://doi.org/10.1016/S0735-1933\(00\)00119-6](https://doi.org/10.1016/S0735-1933(00)00119-6)

- [10] K.M. Becker, Measurements of convective heat transfer from a horizontal cylinder rotating in a tank of water, *Int. J. Heat Mass Transf.*, 6 (1963) 1053-1062. [https://doi.org/10.1016/0017-9310\(63\)90006-1](https://doi.org/10.1016/0017-9310(63)90006-1)
- [11] R.I. Elghnam, Experimental and numerical investigation of heat transfer from a heated horizontal cylinder rotating in still air around its axis, *Ain Shams Eng. J.*, 5 (2014) 177-185. <https://doi.org/10.1016/j.asej.2013.09.008>
- [12] F.K. Tsou, E.M. Sparrow, R.J. Goldstein, Flow and heat transfer in the boundary layer on a continuous moving surface, *Int. J. Heat Mass Transf.*, 10 (1967) 219-235. [https://doi.org/10.1016/0017-9310\(67\)90100-7](https://doi.org/10.1016/0017-9310(67)90100-7)
- [13] K. Gauler, Wärme- und Stoffübertragung an eine mitbewegte Grenzfläche bei Grenzschichtströmung, Dissertation, Universitaet Karlsruhe, 1972
- [14] H. Martin, B. Gampert, G5 Heat Transfer to Single Cylinders, Wires, and Fibers in Longitudinal Flow, in: VDI e.V. (Eds.), *VDI Heat Atlas*, Springer, Berlin, Heidelberg, 2010. https://doi.org/10.1007/978-3-540-77877-6_38
- [15] V. Gnielinski, G2 Heat Transfer in Concentric Annular and Parallel Plate Ducts, in: VDI e.V. (Eds.), *VDI Heat Atlas*, Springer, Berlin, Heidelberg, 2010. https://doi.org/10.1007/978-3-540-77877-6_35
- [16] M. Kind, D. Steiner, J.M. Chawla, J.-J. Schröder, Y. Saito, H. Auracher, O. Herbst, A. Katsaounis, H3 Flow Boiling, in: VDI e.V. (Eds.), *VDI Heat Atlas*, Springer, Berlin, Heidelberg, 2010. https://doi.org/10.1007/978-3-540-77877-6_124
- [17] W. Wagner, H.-J. Kretzschmar, *International Steam Tables - Properties of Water and Steam based on the Industrial Formulation IAPWS-IF97*, Springer, Berlin, Heidelberg, 2008. <https://doi.org/10.1007/978-3-540-74234-0>
- [18] L. Landau, B. Levich, Dragging of a Liquid by a Moving Plate, *Acta Physicochim URSS*, 17 (1942) 42-54.
- [19] N.I. Gel'perin, G.A. Nosov, A.V. Makotkin, Determinating the thickness of liquid film holdup on a rotating drum surface, *Chem. Pet. Eng.*, 11 (1975) 230-233. <https://doi.org/10.1007/BF01146631>
- [20] N. Hasan, J. Naser, Determining the thickness of liquid film in laminar condition on a rotating drum surface using CFD, *Chem. Eng. Sci.*, 64 (2009) 919-924. <https://doi.org/10.18086/swc.2015.02.05>
- [21] Y. Yener, S. Kakaç, *Heat Conduction*, Fourth Edition, Taylor & Francis, New York, Abingdon, 2018. <https://doi.org/10.1201/9780203752166>
- [22] H.D. Baehr, K. Stephan, *Heat and Mass Transfer*, Springer, Berlin, Heidelberg, 2011. <https://doi.org/10.1007/978-3-642-20021-2>
- [23] V. Alexiades, A.D. Solomon, *Mathematical Modeling of Melting and Freezing Processes*, Hemisphere Publishing Corporation, Washington, London, 1993. <https://doi.org/10.1201/9780203749449>
- [24] M.E. Nakhchi, J.A. Esfahani, Improving the melting performance of PCM thermal energy storage with novel stepped fins, *J. Energy Storage*, 30 (2020). <https://doi.org/10.1016/j.est.2020.101424>
- [25] G. Xiaohong, L. Bin, G. Yongxian, Y. Xiugan, Two-dimensional transient thermal analysis of PCM canister of a heat pipe receiver under microgravity, *Appl. Therm. Eng.*, 31 (2011) 735-741. <https://doi.org/10.1016/j.applthermaleng.2010.10.016>
- [26] W.-B. Ye, H.-J. Guo, S.-M. Huang, Y.-X. Hong, Research on melting and solidification processes for enhanced double tubes with constant wall temperature/wall heat flux, *Heat Transf. Asian Res.*, 47 (2018) 583-599. <https://doi.org/10.1002/htj.21328>
- [27] Y. Hong, W.-B. Ye, S.-M. Huang, J. Du, Can the melting behaviors of solid-liquid phase change be improved by inverting the partially thermal-active rectangular cavity?, *Int. J. Heat Mass Transf.*, 126 (2018) 571-578. <https://doi.org/10.1016/j.ijheatmasstransfer.2018.06.012>

- [28] C. Zhang, J. Li, Y. Chen, Improving the energy discharging performance of a latent heat storage (LHS) unit using fractal-tree-shaped fins, *Appl. Energy*, 259 (2020) 114102. <https://doi.org/10.1016/j.apenergy.2019.114102>
- [29] X. Zhang, M. Sheikholeslami, W.-M. Yan, A. Shafee, F. Selimefendigil, H. Babazadeh, Energy storage analysis for discharging of nanoparticle enhanced phase change material within a triplex-tube thermal storage, *J. Energy Storage*, 31 (2020) 101640. <https://doi.org/10.1016/j.est.2020.101640>
- [30] M. Sheikholeslami, S. Lohrasbi, D.D. Ganji, Numerical analysis of discharging process acceleration in LHTESS by immersing innovative fin configuration using finite element method, *Appl. Therm. Eng.*, 107 (2016) 154-166. <https://doi.org/10.1016/j.applthermaleng.2016.06.158>
- [31] A. Abhat, Low temperature latent heat thermal energy storage: Heat storage materials, *Sol. Energy*, 30 (1983) 313-332. [https://doi.org/10.1016/0038-092X\(83\)90186-X](https://doi.org/10.1016/0038-092X(83)90186-X)
- [32] H. Nouredдини, B.C. Teoh, L. Davis Clements, Densities of vegetable oils and fatty acids, *J. Am. Oil Chem. Soc.*, 69 (1992) 1184-1188. <https://doi.org/10.1007/BF02637677>
- [33] D. Rozanna, T.G. Chuah, A. Salmiah, T.S.Y. Choong, M. Sa'ari, Fatty Acids as Phase Change Materials (PCMs) for Thermal Energy Storage: A Review, *Int. J. Green Energy*, 1 (2005) 495-513. <https://doi.org/10.1081/GE-200038722>
- [34] K.W. Hunten, O. Maass, Investigation of Surface Tension Constants in an Homologous Series from the Point of View of Surface Orientation, *J. Am. Chem. Soc.*, 51 (1929) 153-165. <https://doi.org/10.1021/ja01376a018>
- [35] Y. Nagasaka, A. Nagashima, The thermal conductivity of molten NaNO₃ and KNO₃, *Int. J. Thermophys.*, 12 (1991) 769-781. <https://doi.org/10.1007/BF00502404>
- [36] H. Schinke, F. Sauerwald, Dichtemessungen. Über die Volumenänderung beim Schmelzen und den Schmelzprozeß bei anorganischen Salzen, *J. Inorg. Gen. Chem.*, 304 (1960) 25-36. <https://doi.org/10.1002/zaac.19603040104>
- [37] V.M.B. Nunes, M.J.V. Lourenço, F.J.V. Santos, C.A.N. de Castro, Viscosity of Molten Sodium Nitrate, *Int. J. Thermophys.*, 27 (2006) 1638-1649. <https://doi.org/10.1007/s10765-006-0119-1>
- [38] J.L. Dahl, F.R. Duke, Surface Tensions of the AgNO₃-NaNO₃ and AgNO₃-KNO₃ Systems, *The J. Phys. Chem.*, 62 (1958) 1142-1143. <https://doi.org/10.1021/j150567a034>
- [39] J. Stefan, Ueber die Theorie der Eisbildung, insbesondere über die Eisbildung im Polarmeere, *Annalen der Physik*, 278 (1891) 269-286. <https://doi.org/10.1016/j.rser.2006.05.005>
- [40] H.S. Carslaw, J.C. Jaeger, *Conduction of Heat in Solids*, Oxford University Press, Oxford, 1959.
- [41] M. Kenisarin, K. Mahkamov, Solar energy storage using phase change materials, *Renew. and Sustain. Energy Rev.*, 11 (2007) 1913-1965. <https://doi.org/10.1016/j.rser.2006.05.005>
- [42] M.C. Costa, M.P. Rolemberg, L.A.D. Boros, M.A. Krähenbühl, M.G. de Oliveira, A.J.A. Meirelles, Solid-Liquid Equilibrium of Binary Fatty Acid Mixtures, *J. Chem. & Eng. Data*, 52 (2007) 30-36. <https://doi.org/10.1021/je060146z>
- [43] W. Roetzel, B. Spang, C3 Typical Values of Overall Heat Transfer Coefficients, in: VDI e.V. (Eds.), *VDI Heat Atlas*, Springer, Berlin, Heidelberg, 2010. https://doi.org/10.1007/978-3-540-77877-6_6